NANO LETTERS

Letter

pubs.acs.org/NanoLett

Rapid Flame Synthesis of Atomically Thin MoO_3 down to Monolayer Thickness for Effective Hole Doping of WSe_2

Lili Cai,[†] Connor J. McClellan,[‡] Ai Leen Koh,[∥] Hong Li,[†,⊥] Eilam Yalon,[‡] Eric Pop,[‡,#] and Xiaolin Zheng*[,†]

[†]Department of Mechanical Engineering, Stanford University, Stanford, California 94305, United States

[‡]Department of Electrical Engineering, Stanford University, Stanford, California 94305, United States

[∥]Stanford Nano Shared Facilities, Stanford University, Stanford, California 94305, United States

[⊥]School of Mechanical and Aerospace Engineering, Nanyang Technological University, Singapore 639798

[#]Department of Materials Science and Engineering, Stanford University, Stanford, California 94305, United States

Supporting Information

ABSTRACT: Two-dimensional (2D) molybdenum trioxide (MoO_3) with mono- or few-layer thickness can potentially advance many applications, ranging from optoelectronics, catalysis, sensors, and batteries to electrochromic devices. Such ultrathin MoO_3 sheets can also be integrated with other 2D materials (e.g., as dopants) to realize new or improved electronic devices. However, there is lack of a rapid and scalable method to controllably grow mono- or few-layer MoO_3. Here, we report the first demonstration of using a rapid (<2 min) flame synthesis method to deposit mono- and few-layer MoO_3 sheets (several microns in lateral dimension) on a wide variety of layered materials, including mica, MoS_2, graphene, and WSe_2, based on van der Waals epitaxy. The flame-grown ultrathin MoO_3 sheet functions as an efficient hole doping layer for WSe_2, enabling WSe_2 to reach the lowest sheet and contact resistance reported to date among all the p-type 2D materials (~6.5 kΩ/□ and ~0.8 kΩ·μm, respectively). These results demonstrate that flame synthesis is a rapid and scalable pathway to growing atomically thin 2D metal oxides, opening up new opportunities for advancing 2D electronics.

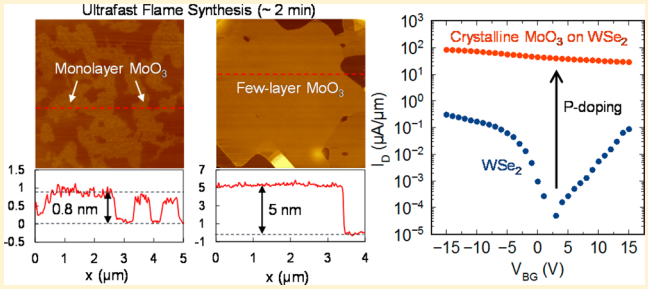

KEYWORDS: *Flame synthesis, MoO_3 monolayer, WSe_2, p-type doping, transition metal dichalcogenides*

Molybdenum trioxide (MoO_3) is a technologically relevant semiconductor with a large electron affinity (>6 eV) and a wide band gap (>3 eV).[1,2] The large electron affinity of MoO_3 makes it an attractive hole dopant for (opto)electronics and the wide band gap makes it transparent. MoO_3 is also used as the active material for catalysis and sensors, and as the electrode in batteries, electrochromic devices, etc.[3−8] Bulk MoO_3 in the orthorhombic phase (α-MoO_3) has a layered structure that stacks covalent-bonded *ac* planes along the *b*-axis direction via van der Waals forces.[9] Compared to its bulk counterpart, two-dimensional (2D) MoO_3 with mono- and few-layer thickness could exhibit different physical and chemical properties (such as band gap, charge transport, and catalytic activity), originating from the confinement in the ultrathin plane.[10] Such thin MoO_3 sheets could also be integrated with other 2D materials into van der Waals heterostructures to realize transparent and flexible 2D devices.[11,12] All these potential applications require the facile synthesis of monolayer or few-layer MoO_3 sheets. To date, only few layers of MoO_3 nanoflakes have been successfully obtained by using mechanical exfoliation,[13] liquid-based exfoliation,[14−16] molecular beam epitaxy,[17] and chemical/physical vapor deposition.[18−20] However, the few-layer MoO_3 nanoflakes produced by these methods have the limitations of small lateral size (50 to 200 nm), slow growth rate, and little control over the thickness or contamination on the surface, which greatly hinders their applications and integration with other 2D materials. In addition, monolayer MoO_3 sheets with lateral size larger than 50 nm have not been realized by these methods, although they in principle are achievable due to the weak van der Waals interaction between layers.[10] There is a great need to develop scalable and fast synthesis routes for the controllable growth of few-layer and even monolayer MoO_3 sheets.

Flame synthesis has demonstrated the advantages of rapid growth rate, low cost, and great scalability.[21−23] It has been widely employed in industry for manufacturing of many commodity zero-dimensional (0D) nanoparticles, such as carbon black, titanium dioxide, and silicon dioxide, and their annual production volume is millions of tons with market value at over $15 billion.[23] In recent years, flame synthesis has also

Received: March 29, 2017
Revised: May 18, 2017
Published: May 24, 2017

ACS Publications © 2017 American Chemical Society

DOI: 10.1021/acs.nanolett.7b01322
Nano Lett. 2017, 17, 3854−3861

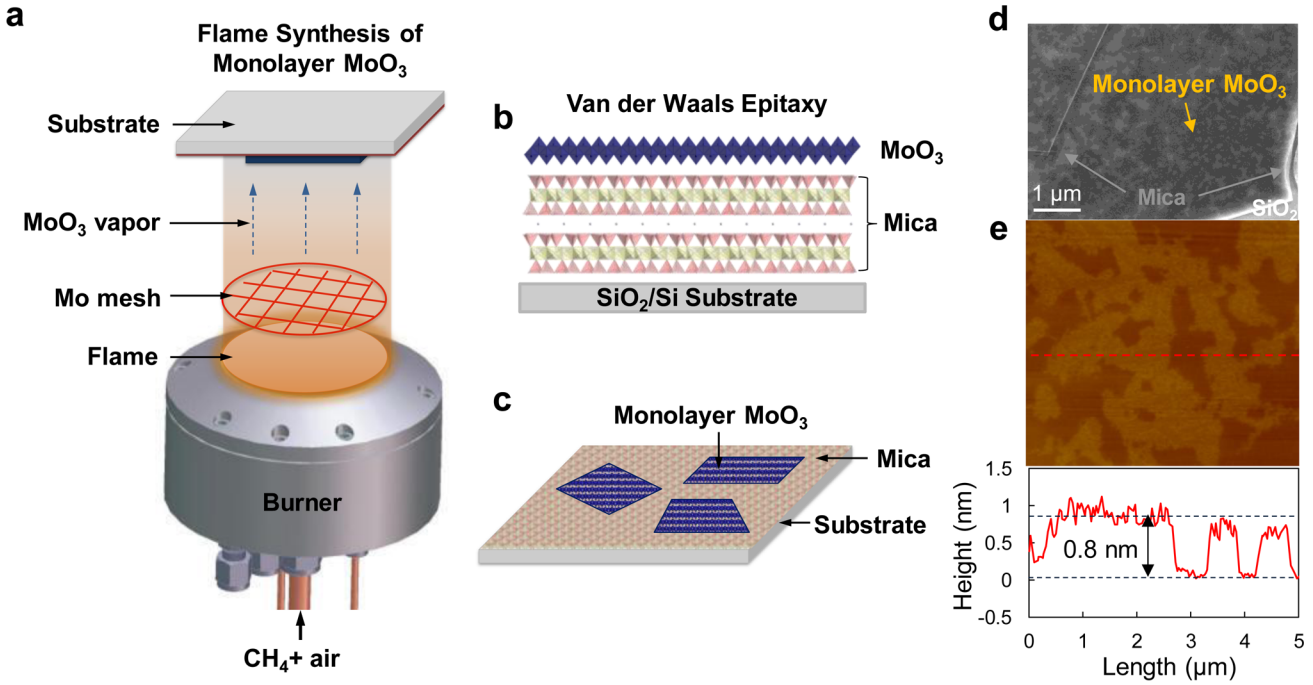

Figure 1. (a) Schematic of the experimental setup for flame synthesis of monolayer MoO_3 on mica. (b) Side-view and (c) top-view schematics showing the van der Waals epitaxial growth of monolayer MoO_3 on mica, supported by a SiO_2/Si substrate. (d) SEM image and (e) AFM image of the monolayer MoO_3 grown on mica. The AFM height profile shows that the thickness of MoO_3 is about 0.8 nm.

been successfully applied to the growth of one-dimensional (1D) metal oxide nanowires, including tungsten oxides,[24,25] molybdenum oxide,[26,27] iron oxides,[28] copper oxide,[29] and zinc oxide.[30,31] Despite the success in flame synthesis of 0D and 1D metal oxides, flame synthesis of 2D metal oxides has not been explored yet.

In this work, we report the first demonstration of using flame synthesis to deposit mono- and few-layer MoO_3 sheets on a wide variety of 2D layered materials, including mica, MoS_2, graphene, and WSe_2, based on a van der Waals epitaxial growth mechanism. Such flame synthesis was accomplished in a short duration of 2 min or less. A key enabling factor for flame synthesis of mono- and few-layer MoO_3 sheets is the ability of this method to achieve very low and tunable O_2 partial pressure (0.01 to 10 Torr). When the flame-grown thin MoO_3 sheets are deposited on top of prefabricated few-layer WSe_2 field-effect transistors (FETs), the ultrathin MoO_3 sheets function as efficient hole doping for WSe_2. The presence of flame-grown MoO_3 sheets greatly reduces the sheet resistance (R_{SH}, from ~900 to 6.5 kΩ/□) and contact resistance (R_C, from ~100 to 0.8 kΩ·μm) of WSe_2. These reduced R_{SH} and R_C values are among the lowest reported for p-type transition metal dichalcogenide (TMD) materials (R_{SH} = 7.4 to 17.0 kΩ/□ and R_C = 1.3 to 11.5 kΩ·μm).[32,33,38,39] The final MoO_3/WSe_2 heterostructure achieves an ultrahigh current density up to 1 mA/μm and good air stability over 20 days, contrasting many other 2D material doping techniques, which degrade over a matter of hours or a few days.[39,41] This work demonstrates the great potential of using flame synthesis to deposit atomically thin 2D metal oxides and to further use those oxides for electronic applications.

The experimental setup for the flame synthesis of MoO_3 monolayers is schematically illustrated in Figure 1a. The flame synthesis setup, from bottom to top, consists of a premixed flat flame burner, a molybdenum (Mo) metal mesh as the precursor source, and exfoliated thin mica flakes supported on a SiO_2/Si wafer as the growth substrate. The premixed burner runs on CH_4 (fuel) and air (oxidizer) that generate a flat premixed flame on the top surface of the burner. The premixed flame provides O_2 and heat for the oxidation of Mo metal mesh and for the evaporation of Mo oxides. Here, we control the metal source temperature at 590 °C and flame equivalence ratio Φ < 1 (see below for the explanation of flame equivalence ratio) to promote the selective formation and evaporation of MoO_3, instead of MoO_2 or other substoichiometric Mo oxides.

The MoO_3 vapor condenses on the mica growth substrate (on a SiO_2/Si wafer, see Methods) placed downstream in a lower temperature region at 450 °C. The mica (muscovite) surface is atomically flat and has been used as an ideal substrate for the van der Waals epitaxial growth of crystalline 1D nanowires[42] and 2D nanomaterials.[19,43] The use of van der Waals layered materials, such as mica, as growth templates is key for growing horizontally aligned 2D MoO_3 layers. The van der Waals interaction between the growth template and MoO_3 relaxes their lattice mismatch, thus inducing van der Waals epitaxial growth of 2D MoO_3. The growth substrate here is different from our previous work, which used substrates including Si, metal, and glass.[27] Those substrates have surface dangling bonds, leading to the growth of perpendicularly aligned 1D MoO_3 nanobelts along [001] direction. In our setup, we also control the postflame O_2 partial pressure to be low so that monolayer crystalline MoO_3 is grown on top of the mica surface (Figure 1b,c). A typical growth time is 2 min (shorter growth time results in sparse deposition and longer time results in thicker film deposition), which is significantly shorter than those of previous van der Waals epitaxy approaches using a hot plate (10 to 60 min)[19] and of ambient pressure physical vapor deposition (over an hour).[20]

The as-grown MoO_3 on mica/SiO_2/Si was first examined using scanning electron microscopy (SEM). As shown in Figure

DOI: 10.1021/acs.nanolett.7b01322
Nano Lett. 2017, 17, 3854−3861

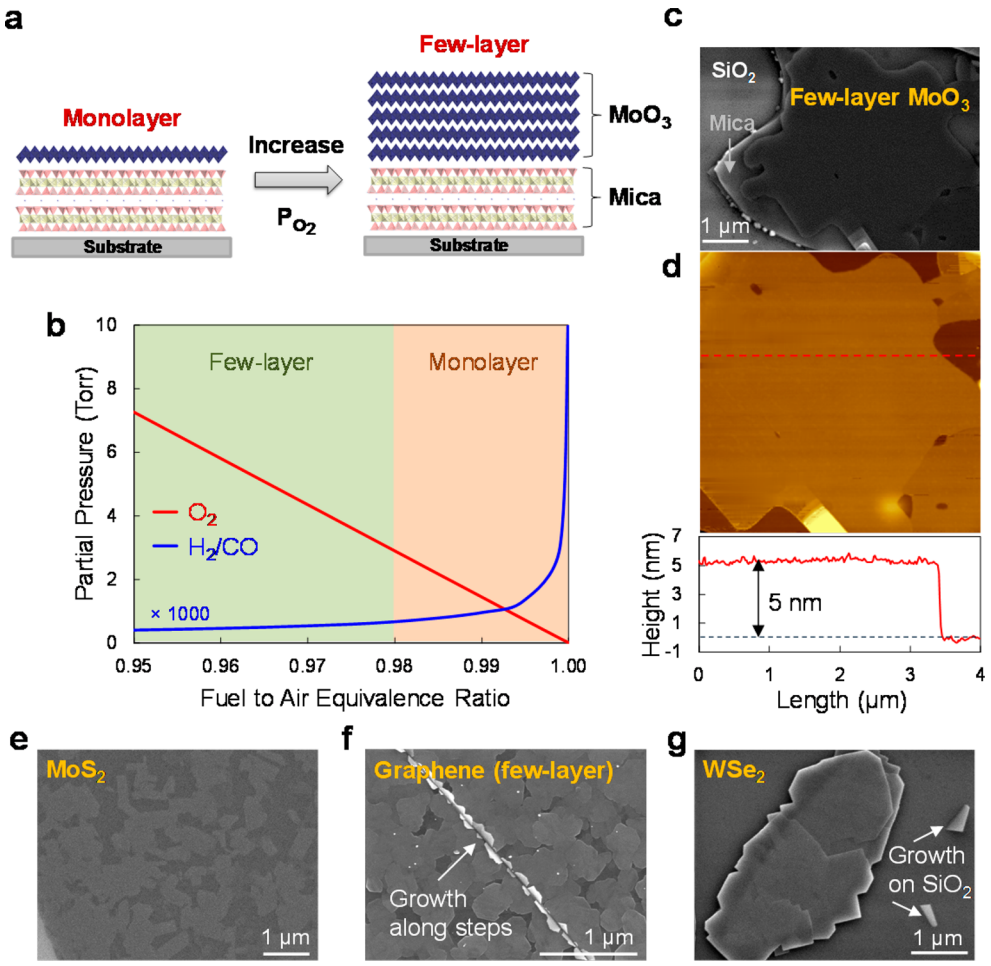

Figure 2. (a) Schematic showing the effect of O_2 partial pressure on the MoO_3 thickness. (b) Plots of O_2, H_2, and CO partial pressures in the postflame region versus flame fuel to air equivalence ratio. H_2 and CO lines are overlapping as they have the same profile. (c) SEM image and (d) AFM image of the few-layer MoO_3 on mica. The AFM height profile shows that the thickness of MoO_3 is about 5 nm. SEM images of the few-layer MoO_3 grown on (e) monolayer MoS_2, (f) few-layer graphene, and (g) few-layer WSe_2 via van der Waals epitaxy. In contrast to the horizontal growth of MoO_3 on the basal plane of layered materials, MoO_3 grows vertically along the steps of few-layer graphene and on SiO_2.

1d, the mica flakes on top of SiO_2 appear to be flat and greyish with bright edges. A large portion of the mica surface appears to be blackish, corresponding to the as-grown MoO_3 with a lateral size of several microns. The brightness contrast between the MoO_3 layer (black) and the mica (gray) under SEM indicates that MoO_3 is slightly more conductive than mica, consistent with the fact that MoO_3 is a wide bandgap semiconductor and mica is an insulator. Further atomic force microscopy (AFM) measurement (Figure 1e) shows that the as-grown MoO_3 layer has a uniform thickness of ~0.8 nm. Note that the *b* lattice constant of a MoO_3 unit cell is 1.4 nm, and each unit cell contains two MoO_3 layers along the *b* axis. Therefore, this AFM result indicates that the as-grown MoO_3 is a monolayer. It should be noted that the previously reported thinnest MoO_3 sheet with lateral size larger than 50 nm was 1.4 nm, corresponding to two MoO_3 layers.[20] Hence, our flame synthesis is the first successful growth of MoO_3 monolayer flake of several microns in lateral dimension, and the growth is uniform over a centimeter size substrate.

In addition to monolayers, few-layer or even thicker MoO_3 sheets can be flame synthesized by increasing the O_2 partial pressure in the postflame region surrounding the Mo mesh (Figure 2a). Normally, lower O_2 partial pressure leads to slow oxidation of the Mo metal and a lower concentration of MoO_3 vapor, which leads to the growth of MoO_3 monolayers. Conversely, higher O_2 partial pressure leads to the growth of few-layer and even thicker MoO_3. The partial pressures of the post flame O_2 and other reducing gaseous species, such as CO and H_2, are controlled by the flame fuel-to-air equivalence ratio (Φ). The ratio Φ is defined as the actual fuel/oxygen molar ratio normalized by the stoichiometric fuel/oxygen molar ratio. Experimentally, Φ is varied by changing the flow rates of CH_4 (fuel) and air (oxidizer). The calculated equilibrium partial pressures of postflame O_2, H_2, and CO (STANJAN software) are plotted as a function of equivalence ratio Φ in Figure 2b. When Φ is very close to 1, CH_4 and O_2 react almost completely to form CO_2 and H_2O, so the partial pressure of the post flame O_2 is very low. As Φ decreases, there is more than sufficient air to burn CH_4 so the partial pressure of the post flame O_2 increases. The trend of the partial pressures of the reducing gaseous species H_2 and CO is the opposite. Experimentally, we found that MoO_3 monolayers are grown on mica when Φ = 0.99 (Figure 1d) and MoO_3 few-layers were grown when Φ = 0.96 (Figure 2c). The AFM image in Figure 2d shows that these MoO_3 layers have a uniform thickness of ~5 nm, representing approximately 6−8 layers. These results show that the thickness of the MoO_3 sheet can be varied by changing Φ, which can be conveniently controlled in our experiments.

DOI: 10.1021/acs.nanolett.7b01322
Nano Lett. 2017, 17, 3854−3861

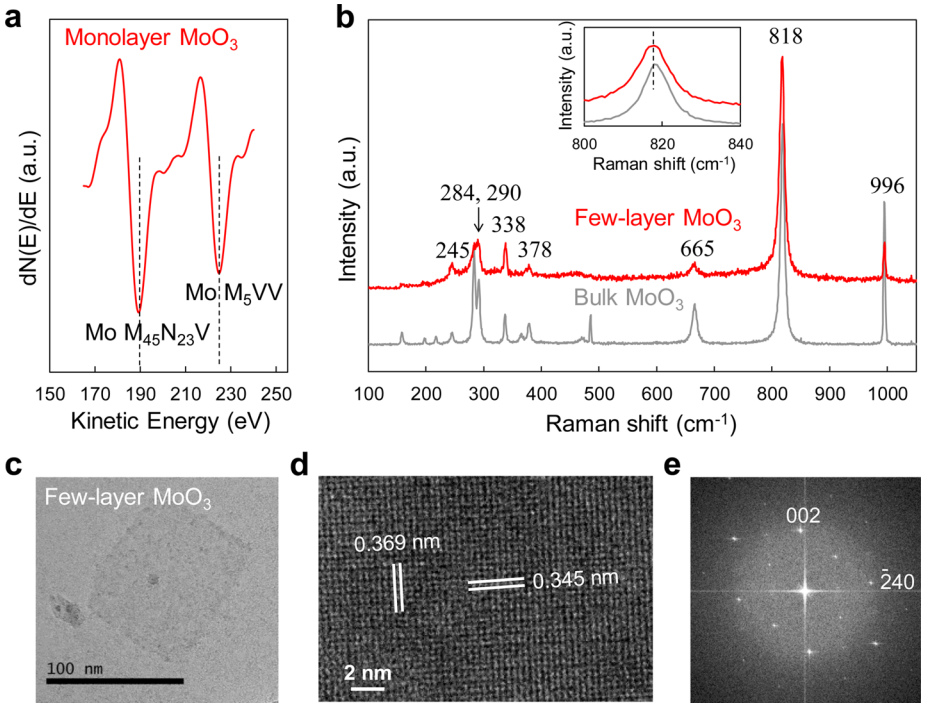

Figure 3. (a) Auger spectrum of monolayer MoO_3 grown on mica in derivative mode plotted as a function of kinetic energy. (b) Raman spectra of the few-layer and bulk MoO_3 grown on few-layer graphene. The inset shows the zoom-in of the peak at 818 cm^{-1}. (c) Low- and (d) high-resolution TEM images and (e) corresponding FFT pattern of the few-layer MoO_3 grown on one- to two-layer graphene.

Similar flame synthesis of MoO_3 few-layers can be extended by using other 2D materials as the epitaxial growth templates, including monolayer MoS_2, few-layer graphene, and few-layer WSe_2, as shown in Figure 2e–g. The basal planes of the as-deposited MoO_3 sheets are parallel to these 2D material substrates, suggesting a similar van der Waals epitaxy mechanism. In comparison, MoO_3 sheets grow vertically along the *steps* of the few-layer graphene sheets (Figure 2f) and on the SiO_2 substrate (Figure 2g), where the surfaces are not atomically flat and dangling bonds exist. This vertical growth behavior is the same as that in our previous study, where MoO_3 tends to grow vertically along [001] direction on Si, metal, and glass substrates to minimize the surface energy.[27]

Next, the flame-grown MoO_3 monolayer and few-layers were characterized using Auger electron spectroscopy (AES), Raman spectroscopy, and transmission electron microscopy (TEM). Figure 3a shows the differentiated AES spectrum at the surface of the flame-grown MoO_3 monolayers on mica. The two Auger peaks at 189 and 225 eV correspond well to the characteristic Mo $M_{45}N_{23}V$ and Mo M_5VV Auger transitions. The Auger peaks confirm the existence of Mo element in the as-grown 2D layers. For the Raman spectroscopy, since mica has many background peaks, MoO_3 few-layers were grown on top of few-layer graphene on Au (300 nm) on our SiO_2/Si substrates (see Methods), which had no background peaks in the Raman shift region of 100 to 1000 cm^{-1}. The as-grown MoO_3 sheets on graphene are typically few layers with a thickness of 2 to 12 nm (Figure 2f). The Raman spectra of these MoO_3 few-layers on graphene exhibit peaks at 245, 248, 290, 338, 378, 665, 818, and 996 cm^{-1} (Figure 3b).[44] All these peak positions are in good agreement with those of bulk orthorhombic α-MoO_3. Notably, the peak at 996 cm^{-1} arises from the asymmetric Mo═O stretching along the *b*-axis direction (out-of-plane), and this peak for the few-layer MoO_3 is relatively weak. The peak at 818 cm^{-1} arises from the symmetric Mo–O–Mo stretching along the *a*-axis direction (in-plane),[44] and this peak for the few-layer MoO_3 sample is relatively strong. These peak intensity changes are consistent with the epitaxial growth orientation along the *b*-axis of MoO_3 since the out-of-plane vibration being parallel to the optical path has a small scattering cross-section, but the in-plane vibration being perpendicular to the optical path has a large scattering cross-section.[45] In addition, the 818 cm^{-1} peak of the few-layer sample is slightly red-shifted compared to that of the bulk sample, suggesting in-plane lattice expansion of the few-layer sample (Figure 3b, inset). Finally, the narrow 996 cm^{-1} peak and the strong and sharp 818 cm^{-1} peak indicate good crystallinity of the flame-grown MoO_3 few layers.[44] In the meantime, we observed that the intensity ratio between the two wagging modes of the terminal Mo═O_1 at 284 cm^{-1} (B_{2g}) and 290 cm^{-1} (B_{3g}) for the few-layer MoO_3 is much lower than that for bulk MoO_3. According to previous studies, this ratio reduction reflects the broken symmetry induced by the oxygen vacancies,[46] suggesting higher content of oxygen vacancies in the few-layer MoO_3 than bulk.

The flame-grown MoO_3 few-layers on graphene (one to two layers) were further characterized by TEM. The low magnification TEM image (Figure 3c) shows that the flame-grown few-layer MoO_3 on graphene is square and rather transparent, suggesting that MoO_3 sheets on graphene are very thin. The high-resolution TEM image (Figure 3d) shows that MoO_3 sheets on graphene exhibit clear lattice fringe patterns, confirming their high crystallinity. The measured lattice distances are 0.369 and 0.345 nm, which match with those of (001) and (120) planes of α-MoO_3, respectively. The TEM results support the above Raman results (Figure 3b) in that flame-grown MoO_3 few-layers on graphene are in the orthorhombic α-MoO_3 phase.[27] The fast Fourier transform (FFT) pattern reveals that the MoO_3 few-layers were imaged

DOI: 10.1021/acs.nanolett.7b01322
Nano Lett. 2017, 17, 3854–3861

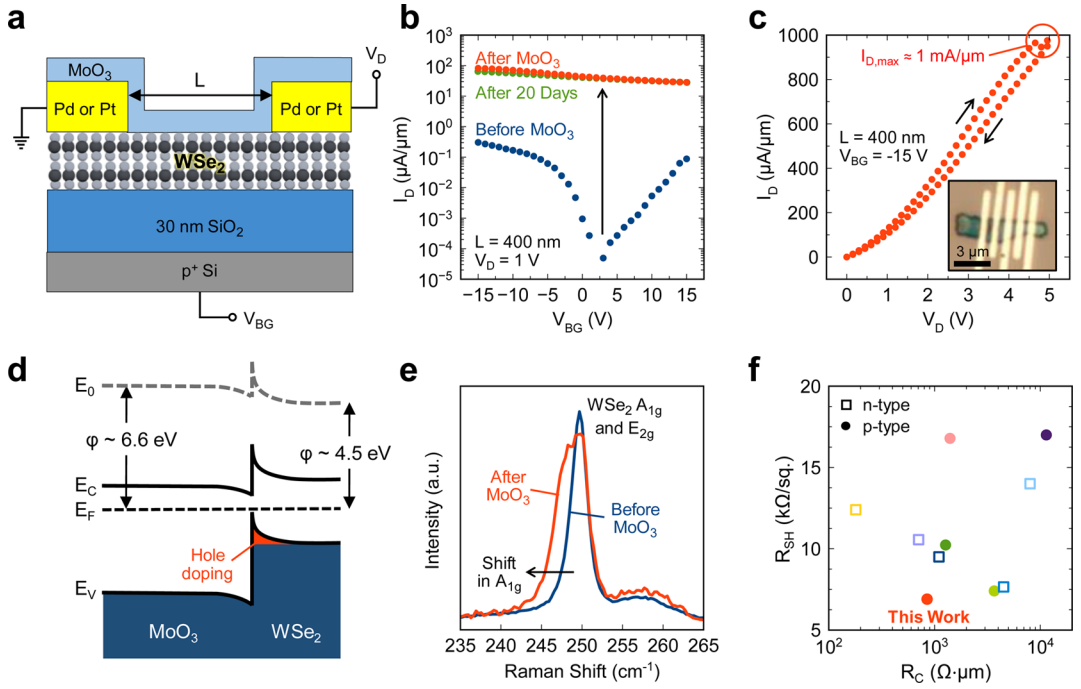

Figure 4. (a) Schematic of the MoO_3-doped WSe_2 transistor. (b) Transfer characteristics of the WSe_2 FET before and after MoO_3 deposition, and after 20 days in air with SiO_2 capping. (c) Output characteristics of the MoO_3-doped WSe_2 device achieving 1 mA/μm. Inset shows optical image of the WSe_2 device after MoO_3 deposition. (d) Schematic of MoO_3/WSe_2 heterojunction showing hole doping effect induced by charge transfer. Band bending in WSe_2 is illustrative of "thick" samples, while ultrathin samples will be fully hole-doped. (e) Raman spectroscopy of the WSe_2 sheet before and after MoO_3 deposition showing a red shift of the A_{1g} peak after MoO_3 deposition. (f) Comparative plot of reported sheet resistance and contact resistance for MoS_2 and WSe_2 using different doping methods. The n-type values are extracted from refs 34–37 and 40, and p-type values are extracted from refs 32, 33, 38, and 39.

along the [210] zone-axis (Figure 3e), which is different from the epitaxial growth orientation of the [010] zone-axis. This difference is due to the difficulty in aligning the basal plane of the ultrathin MoO_3 layers to be perpendicular to the electron beam. In addition, the ultrathin MoO_3 layers undergo a rapid structural change within a few seconds under the radiation of electron beam at a dose rate of 50 $e^-/Å^2{\cdot}s$ (Figure S1).

Next, we used flame synthesis to deposit MoO_3 few-layers onto WSe_2 field-effect transistors (FETs) to study the effects on hole doping (Figure 4a). In this case, the WSe_2 FETs were prefabricated by first transferring WSe_2 flakes (~4 nm thick) onto SiO_2 (30 nm) on p^+ Si substrates, then defining contacts by electron beam lithography, and Pt or Pd physical vapor deposition (PVD), followed by lift-off. Note that we used both Pt and Pd contacts for their large work function but did not observe a quantitative difference between them. Then, the exposed top surface of WSe_2 was covered with a thin layer of MoO_3 by flame synthesis. Before the deposition of MoO_3, all WSe_2 transistors display highly ambipolar behavior (Figure 4b), which is typically observed with Pt or Pd contacts on WSe_2 due to metal work function pinning near the middle of the WSe_2 band gap.[47,48] We also construct transfer length method (TLM)[49] devices with WSe_2 channel lengths from 300 to 700 nm, as shown in Figure S2. Both the extracted sheet and contact resistances of the initial WSe_2 devices at a carrier density of ~7×10^{12} cm^{-2} are high, with $R_S \approx 900$ kΩ/□ and $R_C \approx 100$ kΩ·μm, respectively (Figure S2), leading to poor device performance.

However, after depositing MoO_3, the WSe_2 device displays p-type behavior and the current drive is increased by over 2 orders of magnitude (Figure 4b). We observe this doping effect on numerous WSe_2 devices by varying MoO_3 thickness from 2.5 to 30 nm, with 30 nm showing a slight increase in doping over 2.5 nm thick MoO_3. A large reduction in gate dependence from the doping reduces the max on/off current from ~10^4 to ~10, while the current density reaches as high as 1 mA/μm for the ~4 nm thick WSe_2 device (Figure 4c). Our MoO_3-doped WSe_2 has the highest hole current drive among all the multilayer TMD devices reported to date. We confirm that the increased current is not caused by conduction through the MoO_3 layer with electrical measurements detailed in Figure S3, indicating that the stoichiometric and crystalline epitaxial MoO_3 here is not sufficiently conductive. The TLM extracted R_{SH} and R_C values for the MoO_3-doped WSe_2 at a carrier density of 2×10^{13} cm^{-2} achieve ~6.5 kΩ/□ and ~0.8 kΩ·μm, respectively (Figure S2). Compared to the undoped WSe_2 devices, this 100- to 250-fold reduction in R_{SH} and R_C is caused by the hole doping effect from MoO_3 to WSe_2.

As illustrated in Figure 4d, MoO_3 has a large work function of 6.6 eV,[4] thus a realignment of the WSe_2 and MoO_3 Fermi levels occurs at their interface, which leads to substantial hole doping to the top WSe_2 layers. In addition, the Raman spectroscopy of WSe_2 shows a red shift (~1 cm^{-1}) of the A_{1g} peak after the MoO_3 deposition, leading to a splitting of the otherwise degenerate E_{2g} and A_{1g} peaks (Figure 4e). This A_{1g} peak shift indicates hole doping as observed in previous TMD doping studies.[40,50] We estimate the induced hole density after flame-deposition of MoO_3 to be 2×10^{13} to 5×10^{13} cm^{-2} (Figure S4) using the equation $\Delta p = C_{ox}\Delta V_T/q$, where Δp is the induced hole density, C_{ox} is the oxide capacitance of 30 nm SiO_2, q is the elementary charge, and ΔV_T is the change in threshold voltage.

DOI: 10.1021/acs.nanolett.7b01322
Nano Lett. 2017, 17, 3854–3861

We note that the electrical performance of the MoO_3-doped WSe_2 decreases only slightly after 2 days in air (Figure S5), ostensibly due to a gradual decrease in the MoO_3 work function.[4] In contrast, a previous report using thermally evaporated MoO_3 for p-doping graphene observed a much quicker degradation after only 2 h in air.[51] This suggests that the better stability of our ultrathin MoO_3 sheets in air is due to their crystalline nature, compared to the amorphous and defective films obtained by thermal evaporation. To further improve our device stability, we also employed an additional capping layer of 20 nm SiO_2 deposited by electron-beam evaporation. With this, the electrical performance of our MoO_3-doped WSe_2 devices is relatively stable over 20 days of test, as shown in Figure 4b and Figure S5. In contrast, we note that many other 2D material doping techniques quickly degrade over a few hours or days.[39,41,51]

Lastly, we compare the doping effect on 2D materials of our flame-deposited MoO_3 versus other reported doping methods in terms of the sheet resistance vs contact resistance extracted with TLM (Figure 4f).[32−40] Molecular doping by surface functionalization is currently the most employed doping strategy for TMD transistors, demonstrating sheet and contact resistances of R_{SH} = 7.4 to 10.2 kΩ/□ and R_C = 1.3 to 3.7 kΩ·μm for p-type, R_{SH} = 7.7 to 10.6 kΩ/□ and R_C = 0.7 to 4.5 kΩ·μm for n-type channels.[32−36] However, surface functionalization methods are usually unstable and can have adverse effects on 2D materials, which are very sensitive to surface treatment due to their atomically thin nature.[41,52] For substitutional or vacancy doping, inherent structural damage is common and can result in decreased device mobility, and thus, relatively high sheet resistance (R_{SH} = 14.0 to 17.0 kΩ/□) and contact resistance (R_C = 8.0 to 11.5 kΩ·μm) were observed.[37,38,53] In contrast, the approach employed here involves charge transfer doping by forming oxide/2D material interfaces, offering good chemical stability without damaging the material structure. The reported sheet and contact resistances in previous p-type oxide/2D material studies were higher ($R_{SH} \approx$ 16.8 kΩ/□, $R_C \approx$ 1.4 kΩ·μm).[39] In comparison, our flame-grown MoO_3/WSe_2 heterostructure has advantages of being ultrathin, with good crystallinity and pristine interface, which improve the doping performance. Figure 4f shows that the 2D MoO_3 doping in this work achieved record-low sheet resistance of 6.5 kΩ/□ for a semiconducting TMD at room-temperature and the lowest reported p-type contact resistance of 0.8 kΩ·μm to date. These results demonstrate the great potential of flame-grown ultrathin MoO_3 on other 2D materials to form 2D heterostructures for electronic applications.

In conclusion, we demonstrated the first van der Waals epitaxial growth of 2D MoO_3 down to a monolayer of several microns in lateral dimension over a centimeter size substrate using a rapid flame synthesis method. The MoO_3 growth of such an extreme thickness is enabled by fine control of very low O_2 partial pressure in the flame. In addition, due to the weak van der Waals interaction that relaxes the lattice mismatch, a wide variety of layered or 2D materials, such as mica, MoS_2, graphene, and WSe_2, were used as templates for ultrathin 2D MoO_3 growth, leading to the formation of novel 2D van der Waals heterostructures with pristine interfaces. Acting as a hole doping layer, the ultrathin MoO_3 enables originally ambipolar WSe_2 FETs to show p-type behavior with ultrahigh current drive up to 1 mA/μm and good air stability of more than 20 days (with SiO_2 capping), contrasting the quick doping degradation over a few hours or days observed in other works. The extracted sheet resistance and contact resistance of MoO_3-doped WSe_2 are greatly reduced to ∼6.5 kΩ/□ and 0.8 kΩ·μm, respectively, which are both lower than previous reports for other p-type TMDs. The mono- and few-layer MoO_3 reported here mark new applications of such 2D metal oxides. Our flame approach also provides a rapid and scalable pathway for the production of emerging 2D metal oxides that can open up exciting new opportunities for both fundamental investigations and device applications.

Methods. *Flame Synthesis of Mono- and Few-Layer MoO_3 via van der Waals Epitaxy.* Mono- and few-layer MoO_3 were grown using a 6 cm diameter premixed flat-flame burner (McKenna burner, Holthuis & Associates). The burner operates on CH_4 as the fuel and air as the oxidizer. The flow rate of CH_4 is fixed at 1.84 SLPM, while the flow rate of air varies from 17.70 to 18.25 SLPM (corresponding to flame fuel-to-air equivalence ratio from 0.99 to 0.96), both of which were controlled using mass-flow controllers. A molybdenum mesh was placed in the postflame region above the burner as the source to generate MoO_3 vapor. The temperature of the Mo source mesh was controlled by inserting steel cooling meshes in between the source mesh and the flame. The growth substrates were prepared by mechanical exfoliation and dry transfer of mica, few-layer graphene, and few-layer WSe_2 or chemical vapor deposition (CVD) growth of monolayer MoS_2 on SiO_2 (300 nm)/Si (n-type, 1 to 4 Ω·cm) wafers. The growth substrate was placed in the lower temperature region, and its temperature was controlled by a water-cooled plate on the back. Typical growth conditions were equivalence ratios of 0.99 to 0.96, source temperature of 590 °C, growth temperature of 450 °C, and growth time of 2 min.

Material Characterizations. The as-grown samples were examined using SEM (FEI Sirion XL30, 5 kV), AFM (Park Systems, XE 70), Auger Spectroscopy (PHI 700), Raman spectroscopy (WITEC alpha500, excitation laser of 532 nm), and TEM (FEI Titan, 80 kV). For SEM, AFM, and Auger characterizations, we used mica substrates on SiO_2 (300 nm)/Si (n type, 1 to 4 Ω·cm). For Raman measurement, graphene on Au (300 nm)/SiO_2 (300 nm)/Si (n type, 1 to 4 Ω·cm) substrates were used, which provide no background peaks from the substrates in the Raman shift region below 1000 cm^{-1}. For TEM characterization, graphene TEM support films on lacey carbon (Ted Pella, PELCO, 300 mesh copper grids) were used for direct deposition of mono- and few-layer MoO_3.

Electrical Characterizations. WSe_2 devices were fabricated from WSe_2 flakes exfoliated onto 30 nm SiO_2 thermally grown onto p^+ Si substrates (0.001 to 0.005 Ω·cm). Contacts were patterned using electron-beam lithography with varying channel lengths (0.3 to 2 μm), followed by electron-beam evaporation of Pt or Pd metal contacts. Electrical characterization was performed with a Keithley 4200-SCS parameter analyzer, in a Janis Probe Station under vacuum ($<10^{-4}$ Torr) at room temperature, using the Si substrate as a global back-gate.

■ ASSOCIATED CONTENT

Supporting Information

The Supporting Information is available free of charge on the ACS Publications website at DOI: 10.1021/acs.nanolett.7b01322.

Additional TEM images of MoO_3 and additional electrical characterization results of p-type doping of WSe_2 by MoO_3 (PDF)

DOI: 10.1021/acs.nanolett.7b01322
Nano Lett. 2017, 17, 3854−3861

AUTHOR INFORMATION

Corresponding Author

*E-mail: xlzheng@stanford.edu.

ORCID

Lili Cai: 0000-0003-1222-248X
Connor J. McClellan: 0000-0002-8733-9968
Ai Leen Koh: 0000-0003-1991-100X
Hong Li: 0000-0002-6975-7787
Eilam Yalon: 0000-0001-7965-459X
Eric Pop: 0000-0003-0436-8534
Xiaolin Zheng: 0000-0002-8889-7873

Author Contributions

L.C. and C.J.M. contributed equally to this work. L.C. and X.Z. conceived the study. L.C. carried out material synthesis, SEM characterization, Auger and Raman measurements, and STANJAN calculation. C.J.M. and E.Y. carried out WSe_2 device fabrication and electrical measurements. A.L.K. and L.C. performed TEM characterization and analysis. H.L. and L.C. performed AFM measurement. L.C., C.J.M., and X.Z. wrote the manuscript. X.Z., E.P., L.C., and C.J.M. revised the manuscript. All authors discussed the results and commented on the manuscript.

Notes

The authors declare no competing financial interest.

ACKNOWLEDGMENTS

This work was supported by the Bay Area Photovoltaics Consortium (BAPVC) as well as the 2013 Global Research Outreach (GRO) Program (Award No. IC2012-1318) of the Samsung Advanced Institute of Technology (SAIT) and Samsung R&D Center America, Silicon Valley (SRA-SV) under the supervision of Dr. Debasis Bera and Anthony Radspieler, Jr. We also acknowledge support from the Air Force Office of Scientific Research Award No. FA9550-14-1-0251, the National Science Foundation (NSF) EFRI 2-DARE Grant 1542883, the NSF Graduate Research Fellowship program (to C.J.M.), and the Stanford Initiative for Nanoscale Materials and Processes (INMP). Material characterization was carried out at the Stanford Nano Shared Facility (SNSF) and device fabrication was performed at the Stanford Nanofabrication Facility (SNF).

REFERENCES

(1) Guo, Y.; Robertson, J. *Appl. Phys. Lett.* **2014**, *105* (22), 222110.
(2) Meyer, J.; Kidambi, P. R.; Bayer, B. C.; Weijtens, C.; Kuhn, A.; Centeno, A.; Pesquera, A.; Zurutuza, A.; Robertson, J.; Hofmann, S. *Sci. Rep.* **2015**, *4*, 5380.
(3) Murase, S.; Yang, Y. *Adv. Mater.* **2012**, *24* (18), 2459−2462.
(4) Chuang, S.; Battaglia, C.; Azcatl, A.; McDonnell, S.; Kang, J. S.; Yin, X.; Tosun, M.; Kapadia, R.; Fang, H.; Wallace, R. M.; Javey, A. *Nano Lett.* **2014**, *14* (3), 1337−1342.
(5) Solymosi, F.; Cserenyi, J.; Szoke, A.; Bansagi, T.; Oszko, A. *J. Catal.* **1997**, *165* (2), 150−161.
(6) Eranna, G.; Joshi, B. C.; Runthala, D. P.; Gupta, R. P. *Crit. Rev. Solid State Mater. Sci.* **2004**, *29* (3−4), 111−188.
(7) Chernova, N. A.; Roppolo, M.; Dillon, A. C.; Whittingham, M. S. *J. Mater. Chem.* **2009**, *19* (17), 2526−2552.
(8) Mai, L. Q.; Hu, B.; Chen, W.; Qi, Y. Y.; Lao, C. S.; Yang, R. S.; Dai, Y.; Wang, Z. L. *Adv. Mater.* **2007**, *19* (21), 3712.
(9) Huang, P.-R.; He, Y.; Cao, C.; Lu, Z.-H. *Sci. Rep.* **2015**, *4*, 7131.
(10) Li, F.; Chen, Z. *Nanoscale* **2013**, *5* (12), 5321−5333.
(11) Geim, A. K.; Grigorieva, I. V. *Nature* **2013**, *499* (7459), 419−425.
(12) Huang, X.; Tan, C. L.; Yin, Z. Y.; Zhang, H. *Adv. Mater.* **2014**, *26* (14), 2185−2204.
(13) Kalantar-zadeh, K.; Tang, J.; Wang, M.; Wang, K. L.; Shailos, A.; Galatsis, K.; Kojima, R.; Strong, V.; Lech, A.; Wlodarski, W.; Kaner, R. B. *Nanoscale* **2010**, *2* (3), 429−433.
(14) Balendhran, S.; Walia, S.; Alsaif, M.; Nguyen, E. P.; Ou, J. Z.; Zhuiykov, S.; Sriram, S.; Bhaskaran, M.; Kalantar-zadeh, K. *ACS Nano* **2013**, *7* (11), 9753−9760.
(15) Alsaif, M. M. Y. A.; Balendhran, S.; Field, M. R.; Latham, K.; Wlodarski, W.; Ou, J. Z.; Kalantar-zadeh, K. *Sens. Actuators, B* **2014**, *192*, 196−204.
(16) Sreedhara, M. B.; Matte, H. S. S. R.; Govindaraj, A.; Rao, C. N. R. *Chem. - Asian J.* **2013**, *8* (10), 2430−2435.
(17) Du, Y.; Li, G.; Peterson, E. W.; Zhou, J.; Zhang, X.; Mu, R.; Dohnalek, Z.; Bowden, M.; Lyubinetsky, I.; Chambers, S. A. *Nanoscale* **2016**, *8* (5), 3119−3124.
(18) Deng, X.; Quek, S. Y.; Biener, M. M.; Biener, J.; Kang, D. H.; Schalek, R.; Kaxiras, E.; Friend, C. M. *Surf. Sci.* **2008**, *602* (6), 1166−1174.
(19) Molina-Mendoza, A. J.; Lado, J. L.; Island, J. O.; Niño, M. A.; Aballe, L.; Foerster, M.; Bruno, F. Y.; López-Moreno, A.; Vaquero-Garzon, L.; van der Zant, H. S. J.; Rubio-Bollinger, G.; Agraït, N.; Pérez, E. M.; Fernández-Rossier, J.; Castellanos-Gomez, A. *Chem. Mater.* **2016**, *28* (11), 4042−4051.
(20) Wang, D.; Li, J.-N.; Zhou, Y.; Xu, D.-H.; Xiong, X.; Peng, R.-W.; Wang, M. *Appl. Phys. Lett.* **2016**, *108* (5), 053107.
(21) Allen, P.; Cai, L.; Zhou, L.; Zhao, C.; Rao, P. M. *Sci. Rep.* **2016**, *6*, 27832.
(22) Merchan-Merchan, W.; Saveliev, A. V.; Taylor, A. M. *Nanotechnology* **2008**, *19* (12), 125605.
(23) Trommer, R. M.; Bergmann, C. P. Ceramic Products Produced by FS. In *Flame Spray Technology: Method for Production of Nanopowders*; Springer Berlin Heidelberg: Berlin, Heidelberg, 2015; pp 43−72.
(24) Xu, F.; Tse, S. D.; Al-Sharab, J. F.; Kear, B. H. *Appl. Phys. Lett.* **2006**, *88* (24), 243115−243115.
(25) Rao, P. M.; Zheng, X. *Proc. Combust. Inst.* **2011**, *33* (2), 1891−1898.
(26) Merchan-Merchan, W.; Saveliev, A. V.; Desai, M. *Nanotechnology* **2009**, *20* (47), 475601.
(27) Cai, L.; Rao, P. M.; Zheng, X. *Nano Lett.* **2011**, *11* (2), 872−877.
(28) Rao, P. M.; Zheng, X. *Nano Lett.* **2011**, *11* (6), 2390−2395.
(29) Rao, P. M.; Zheng, X. *Nano Lett.* **2009**, *9* (8), 3001−3006.
(30) Xu, F.; Liu, X.; Tse, S. D.; Cosandey, F.; Kear, B. H. *Chem. Phys. Lett.* **2007**, *449* (1), 175−181.
(31) Height, M. J.; Mädler, L.; Pratsinis, S. E.; Krumeich, F. *Chem. Mater.* **2006**, *18* (2), 572−578.
(32) Zhao, P.; Kiriya, D.; Azcatl, A.; Zhang, C.; Tosun, M.; Liu, Y.-S.; Hettick, M.; Kang, J. S.; McDonnell, S.; Kc, S.; Guo, J.; Cho, K.; Wallace, R. M.; Javey, A. *ACS Nano* **2014**, *8* (10), 10808−10814.
(33) Wang, S.; Zhao, W.; Giustiniano, F.; Eda, G. *Phys. Chem. Chem. Phys.* **2016**, *18* (6), 4304−4309.
(34) Yang, L.; Majumdar, K.; Liu, H.; Du, Y.; Wu, H.; Hatzistergos, M.; Hung, P. Y.; Tieckelmann, R.; Tsai, W.; Hobbs, C.; Ye, P. D. *Nano Lett.* **2014**, *14* (11), 6275−6280.
(35) Kiriya, D.; Tosun, M.; Zhao, P.; Kang, J. S.; Javey, A. *J. Am. Chem. Soc.* **2014**, *136* (22), 7853−7856.
(36) Du, Y.; Liu, H.; Neal, A. T.; Si, M.; Ye, P. D. *IEEE Electron Device Lett.* **2013**, *34* (10), 1328−1330.
(37) Tosun, M.; Chan, L.; Amani, M.; Roy, T.; Ahn, G. H.; Taheri, P.; Carraro, C.; Ager, J. W.; Maboudian, R.; Javey, A. *ACS Nano* **2016**, *10* (7), 6853−6860.
(38) Chien, P. Y.; Zhang, M.; Huang, S. C.; Lee, M. H.; Hsu, H. R.; Ho, Y. T.; Chu, Y. C.; Jong, C. A.; Woo, J. Reliable doping technique for WSe_2 by W:Ta co-sputtering process. In *2016 IEEE Silicon Nanoelectronics Workshop (SNW)*, 12−13 June 2016; pp 58−59.
(39) Yamamoto, M.; Nakaharai, S.; Ueno, K.; Tsukagoshi, K. *Nano Lett.* **2016**, *16* (4), 2720−2727.

DOI: 10.1021/acs.nanolett.7b01322
Nano Lett. 2017, 17, 3854−3861

(40) Rai, A.; Valsaraj, A.; Movva, H. C. P.; Roy, A.; Ghosh, R.; Sonde, S.; Kang, S.; Chang, J.; Trivedi, T.; Dey, R.; Guchhait, S.; Larentis, S.; Register, L. F.; Tutuc, E.; Banerjee, S. K. *Nano Lett.* **2015**, *15* (7), 4329−4336.
(41) Yu, L.; Zubair, A.; Santos, E. J. G.; Zhang, X.; Lin, Y.; Zhang, Y.; Palacios, T. *Nano Lett.* **2015**, *15* (8), 4928−4934.
(42) Utama, M. I. B.; Belarre, F. J.; Magen, C.; Peng, B.; Arbiol, J.; Xiong, Q. *Nano Lett.* **2012**, *12* (4), 2146−2152.
(43) Wang, Q.; Safdar, M.; Xu, K.; Mirza, M.; Wang, Z.; He, J. *ACS Nano* **2014**, *8* (7), 7497−7505.
(44) Seguin, L.; Figlarz, M.; Cavagnat, R.; Lassègues, J. C. *Spectrochim. Acta, Part A* **1995**, *51* (8), 1323−1344.
(45) Yan, B.; Zheng, Z.; Zhang, J.; Gong, H.; Shen, Z.; Huang, W.; Yu, T. *J. Phys. Chem. C* **2009**, *113* (47), 20259−20263.
(46) Dieterle, M.; Weinberg, G.; Mestl, G. *Phys. Chem. Chem. Phys.* **2002**, *4* (5), 812−821.
(47) Movva, H. C. P.; Rai, A.; Kang, S.; Kim, K.; Fallahazad, B.; Taniguchi, T.; Watanabe, K.; Tutuc, E.; Banerjee, S. K. *ACS Nano* **2015**, *9* (10), 10402−10410.
(48) Das, S.; Appenzeller, J. *Appl. Phys. Lett.* **2013**, *103* (10), 103501.
(49) English, C. D.; Shine, G.; Dorgan, V. E.; Saraswat, K. C.; Pop, E. *Nano Lett.* **2016**, *16* (6), 3824−3830.
(50) Chakraborty, B.; Bera, A.; Muthu, D. V. S.; Bhowmick, S.; Waghmare, U. V.; Sood, A. K. *Phys. Rev. B: Condens. Matter Mater. Phys.* **2012**, *85* (16), 161403.
(51) Xie, L.; Wang, X.; Mao, H.; Wang, R.; Ding, M.; Wang, Y.; Özyilmaz, B.; Loh, K. P.; Wee, A. T. S.; Ariando; Chen, W. *Appl. Phys. Lett.* **2011**, *99* (1), 012112.
(52) Ghatak, S.; Pal, A. N.; Ghosh, A. *ACS Nano* **2011**, *5* (10), 7707−7712.
(53) McDonnell, S.; Addou, R.; Buie, C.; Wallace, R. M.; Hinkle, C. L. *ACS Nano* **2014**, *8* (3), 2880−2888.

DOI: 10.1021/acs.nanolett.7b01322
Nano Lett. 2017, 17, 3854−3861

Supporting Information

Rapid Flame Synthesis of Atomically Thin MoO_3 down to Monolayer Thickness for Effective Hole Doping of WSe_2

Lili Cai,[†,§] Connor J. McClellan,[‡,§] Ai Leen Koh,[‖] Hong Li,[†,⊥] Eilam Yalon,[‡] Eric Pop,[‡,#] and Xiaolin Zheng*[†]

[†]Department of Mechanical Engineering, Stanford University, Stanford, California 94305, USA

[‡]Department of Electrical Engineering, Stanford University, Stanford, California 94305, USA

[‖]Stanford Nano Shared Facilities, Stanford University, Stanford, California 94305, USA

[⊥]School of Mechanical and Aerospace Engineering, Nanyang Technological University, Singapore 639798

[#]Department of Materials Science and Engineering, Stanford University, Stanford, California 94305, USA

§These authors contributed equally

*Corresponding author: xlzheng@stanford.edu

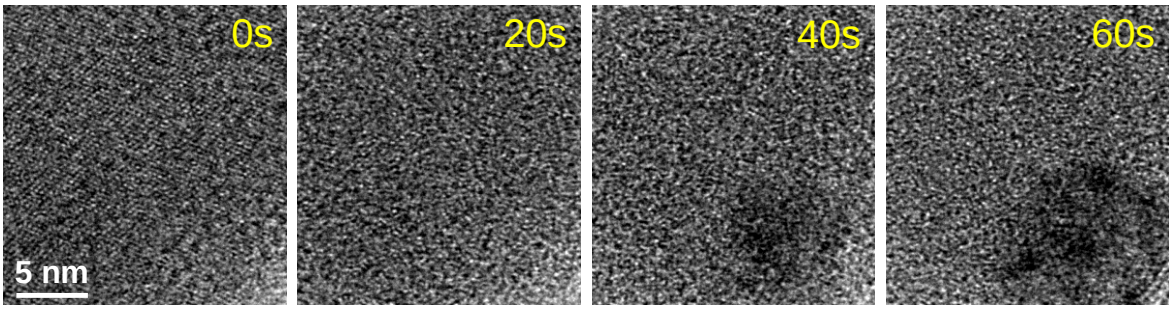

Figure S1. TEM images of MoO_3 thin layers over a duration of 60 s, showing that its crystalline structure was quickly damaged under the radiation of electron beam.

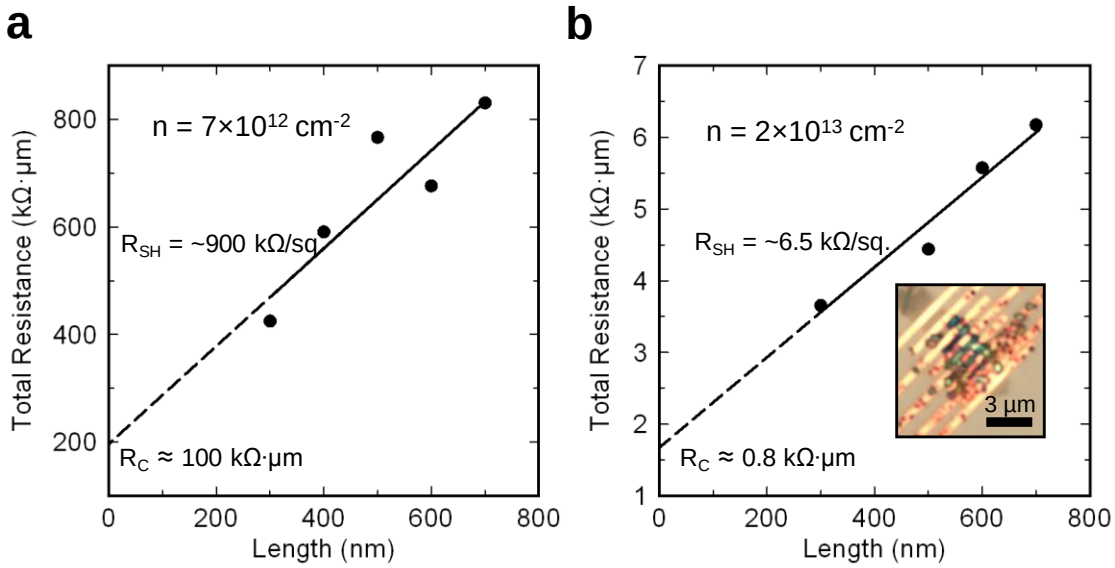

Figure S2. Transfer length method (TLM) extraction of sheet resistance (R_{SH}) and contact resistance (R_C) (a) before and (b) after MoO_3 deposition. R_{SH} is equal to the slope of the total resistance vs. length fit and $2R_C$ is equal to the y-intercept. Inset of (b) shows the TLM device used in this work. The color variation on the device is due to the MoO_3 deposition on Pt contacts. In contrast, the device in Figure 4c looks uniform as MoO_3 does not deposit on Pd contacts. We note that achieving both low R_{SH} and R_C details the accuracy of our TLM extraction as underestimated extractions of R_C will result in overestimations of R_{SH} (and vice versa).

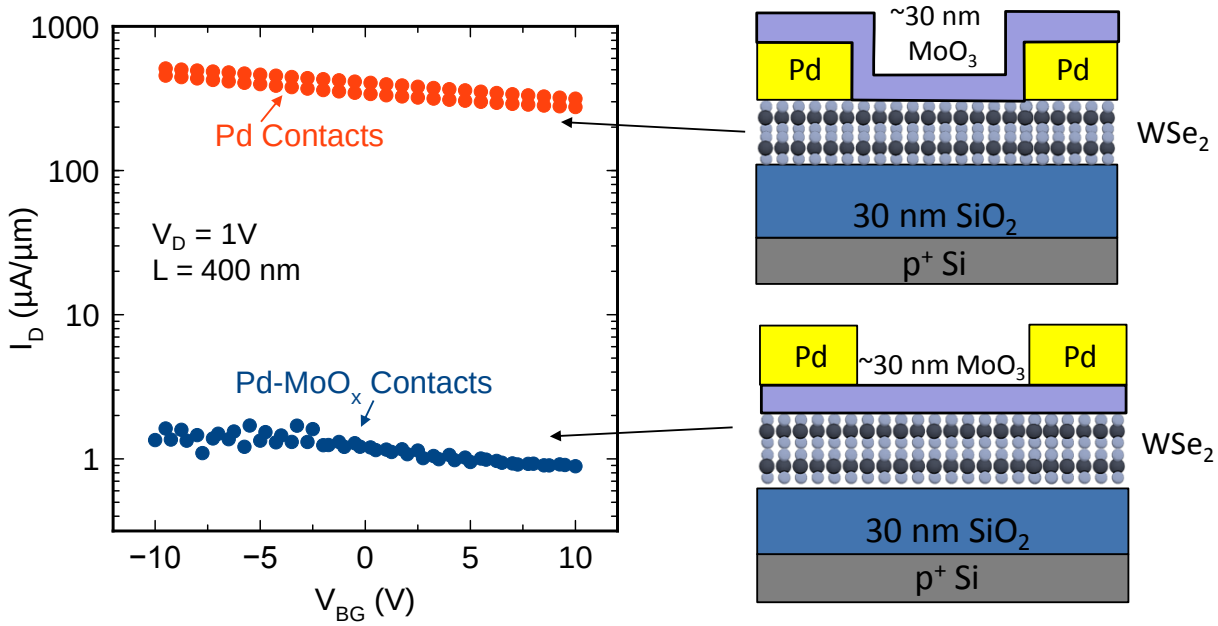

Figure S3. Comparison of Pd-MoO_3 and Pd-WSe_2 contacts. We note substoichiometric MoO_x is often used as a hole injection layer in semiconductor devices, and we first speculated this change in electrical conductivity after MoO_3 deposition could be a result of highly conductive MoO_x. We confirm insulating MoO_3 with electrical measurements by depositing Pd contacts on top of MoO_3 to create Pd-MoO_3 contacts to WSe_2. I-V results of the Pd-MoO_3 contacts demonstrate 100x less conduction than a Pd contacted WSe_2 FET on the same WSe_2 flake, suggesting the MoO_3 deposited in this study is not highly conductive**.**

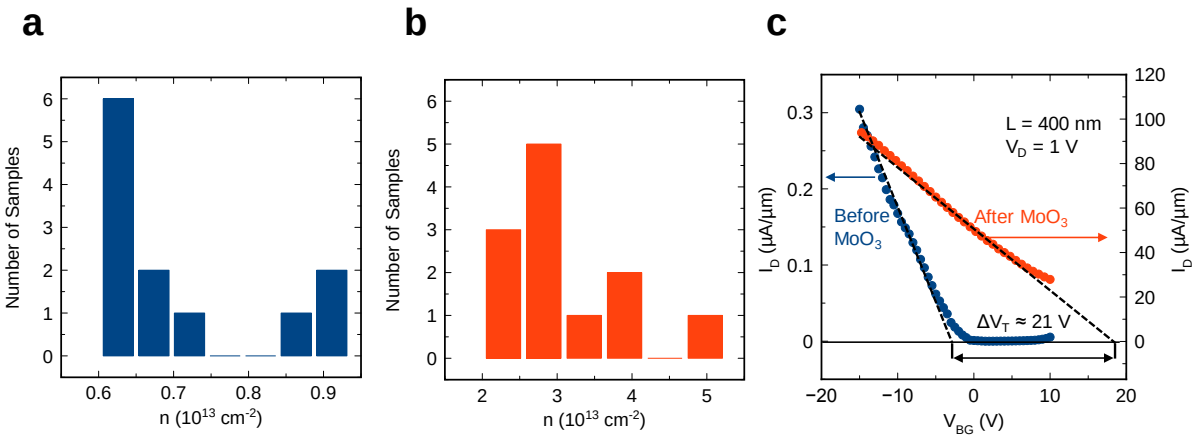

Figure S4. Plot of number of samples vs. carrier concentration at V_{BG} = 20 V for WSe_2 FETs (a) before and (b) after MoO_3 deposition. (c) Example of V_T extraction from linear I_D-V_{BG} data. A large increase in carrier concentration is observed for 12 different samples. The carrier concentration is extracted using the equation: $p = C_{ox}(V_{BG} - V_T)/q$, where C_{ox} is the gate oxide capacitance, V_{BG} is the gate voltage (20 V in this plot), q is the elementary charge and V_T is the threshold voltage extracted using the linear extraction method.

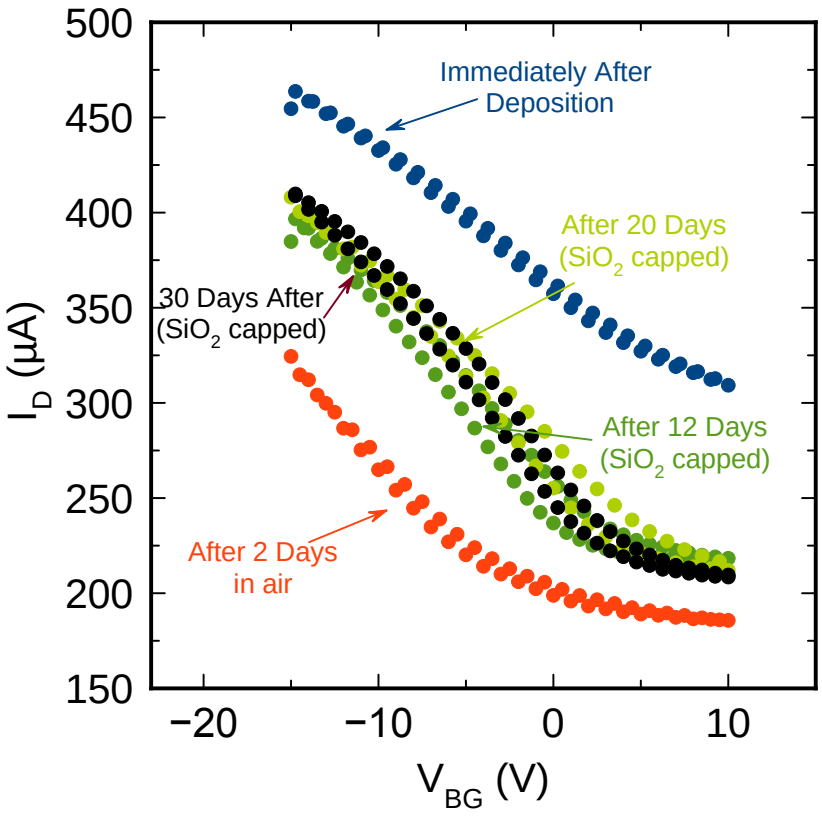

Figure S5. Current vs. gate voltage plot of a device showing change in doping effect over time. After 2 days in air, the current drive decreased most likely due to the surface contaminates on MoO_3. After capping the MoO_3/WSe_2 FET with PVD SiO_2, the device remained relatively stable over 30 days. The slight increase of current drive after PVD SiO_2 can be attributed to the decrease in carbon contamination from the low deposition pressure for SiO_2.